Investigating the origin of photoplethysmography using a multiwavelength Monte Carlo model

Subhasri Chatterjee, Karthik Budidha and Panayiotis A Kyriacou

Research Centre for Biomedical Engineering, City, University of London, UK

E-mail: subhasri.chatterjee.2@city.ac.uk

June 2020

Abstract. Photoplethysmography (PPG) is a photometric technique used for the measurement of volumetric changes in the blood. The recent interest in new applications of PPG has invigorated more fundamental research regarding the origin of the PPG waveform, which since its discovery in 1937, remains inconclusive. A hand full of studies in the recent past have explored various hypotheses for the origin of PPG. These studies relate the PPG to mechanical movement, red blood cell orientation or blood volume variations. Recognising the significance and need to corroborate a theory behind the PPG formation, the present work rigorously investigates the origin of PPG based on a realistic model of light-tissue interactions. A three-dimensional comprehensive Monte Carlo model of finger-PPG was developed and explored to quantify the optical entities pertinent to PPG (e.g., absorbance, reflectance, and penetration depth) as the functions of multiple wavelengths and source-detector separations. Complementary to the simulations, a pilot *in vivo* investigation was conducted on eight healthy volunteers. PPG signals were recorded using a custom-made multi-wavelength sensor with an adjustable source-detector separation. Simulated results illustrate the distribution of photon-tissue interactions in the reflectance PPG geometry. The depth-selective analysis quantifies the contributions of the dermal and subdermal tissue layers in the PPG wave formation. A strong negative correlation (r = -0.96) is found between the ratios of the simulated absorbances and measured PPG amplitudes. This work quantified for the first time the contributions of different tissue layers and sublayers in the formation of the PPG signal.

1. Introduction

Photoplethysmography (PPG) is a non-invasive technique that uses light for measuring the volumetric changes in blood associated with the cardiac cycle in the vascular tissue beds [1]. In PPG, a volume of peripheral tissue is illuminated by optical radiation that undergoes multiple events of scattering and absorption as it traverses through different tissue-layers, and finally is transmitted through or reflected from the tissue volume [2]. Attenuation of light energy is caused by the pulsatile and non-pulsatile components of

the tissue volume and the reflected/ transmitted optical signal is recorded by a sensor as the PPG waveform. It is considered that the pulsatile compartments of the tissue (e.g., arterial blood) give rise to the 'ac' PPG signal that varies with the cardiac cycle, whereas the non-pulsatile compartments of the tissue (e.g., bloodless tissue etc.) give rise to the slowly varying 'dc' PPG signal. A continuous PPG signal is often acquired in current clinical practice using a pulse oximeter which uses PPGs acquired at two wavelengths to measure arterial oxygen saturation (SpO_2) [3, 4].

In recent years, there has been a plethora of interest in extending the application of PPG beyond pulse oximetry, for example, usage of the PPG in the assessment of vascular mechanics, blood pressure, blood viscosity, pulse transit time estimation, pulse rate variability, assessment of tissue perfusion etc. [5–11]. The growing research interest in the PPG applications has raised certain questions regarding the fundamental aspects of PPG, intriguing the researchers to investigate its origin [12–15]. Previous studies have identified some of the key factors to affect the PPG waveform which includes blood volume, blood vessel wall movement, and the orientation of red blood cells; and provided analytical explanation of the light modulation in PPG [16–19]. Recently, the work by Alexei A. Kamshilin *et. al.* has hypothesised the mechanical properties of the capillaries as the major factor for the PPG waveform generation [13], while another study by Andreia V. Moço *et. al.* has considered the volumetric model to analyse the origin of the PPG [12]. Contrary to these studies, Volkov *et. al.* hypothesised that the movement of erythrocytes in capillaries with each cardiac cycle produces profound changes in absorption and hence the PPG waveform [20]. These hypotheses are crucial for profoundly understanding the origin of the PPG, however, to know what gives the PPG waveform its shape and to validate the above hypotheses, it is necessary to perceive the absorbance contributions of all pulsatile and non-pulsatile components of a specific tissue-region of interest (ROI).

Theoretically, the detection of an optical signal by a bio-optical sensor such as PPG relies on the modified Beer-Lambert law [21] which defines the attenuation of light through a medium (A) as a function of the attenuation coefficient (μ) of the medium and the optical pathlength (l) as shown in the Eq. 1:

$$A(\lambda) = \mu(\lambda) \cdot l(\lambda) + G \tag{1}$$

where λ and G are the operating wavelength and the geometry-dependent constant term respectively. Arterial Blood Volume Variation (BVV) occurring with every cardiac cycle within the microvascular bed of tissue is associated with the changes in the optical properties of the tissue. The variations in the attenuation coefficient result in variation in absorbances, affecting the unattenuated optical energy, i.e., the recorded signal by the sensor. Hence, the absorbances at each different depth through the tissue volume should reflect the depth-selective contributions in the formation of a PPG signal.

In order to estimate the contributions of the pulsatile and non-pulsatile tissue compartments in the formation of a PPG waveform, the present work aims to develop a Monte Carlo model of optical interactions within a finger tissue volume. The study

explores the model to quantify the depth-selective absorbances at multiple wavelengths in a reflectance PPG geometry and validate the simulation results through *in vivo* investigations. Monte Carlo models used for PPG analysis in the recent years [12, 22] are limited with several assumptions and simplifications. Also, Monte Carlo models have never been explored for assessing the absorbances pertinent to PPG. The objective of the present work, therefore, is to explore a heterogeneous three-dimensional Monte Carlo model of finger-PPG for the novel multiwavelength analysis of depth-selective absorbances followed by experimental verification.

2. Methodology

The aim of the present work has been achieved through the steps of a Monte Carlo simulation followed by a set of *in vivo* experiments. A comprehensive Monte Carlo model of the finger was developed in our previous study [23] which has been modified with the boundary corrections in this work. The model has been executed in a reflectance geometry at eight wavelengths, namely, 470 nm, 530 nm, 660 nm, 770 nm, 810 nm, 940 nm, 1020 nm and 1050 nm throughout a range of source-detector separations of 1-10 mm. Complementing the simulations, a pilot *in vivo* study has been carried out to acquire and analyse PPG signals from a small group of healthy volunteers at multiple wavelengths (i.e., 460 nm, 525 nm, 640 nm, 770 nm, 810 nm, 940 nm, 1020 nm and 1050 nm) through the source-detector separations of 1-10 mm.

2.1. Monte Carlo model

2.1.1. Anatomical feature The anatomical features of the model are illustrated in Figure 1. The overall geometry of the volume of the index finger was presented by a three-dimensional slab. The volume of the index finger had a thickness of 1.3 cm, a width of 1.3 cm and a semi-infinite length. The heterogeneous tissue volume contained the layers [24–30]: skin sublayers, fat, muscle, and then fat and skin sublayers in the reverse order. The muscle layer contained a cylindrical bone of a diameter of 4 mm at a depth of 5 mm from the top surface. The muscle layer was considered 10 mm thick and represented the overall fibrous tissue-network surrounding the bone such as tendons and ligaments (e.g., annular pulleys and cruciate pulleys) that are attached to the lumbrical muscle [27, 31, 32]. The skin layer had a total thickness of 0.95 mm [30,33] and comprised six sublayers [26,34–36]: (1) stratum corneum, (2) epidermis, (3) papillary dermis, (4) upper blood net dermis, (5) reticular dermis and (6) deep blood net dermis. In table 1, the six sublayers of skin with their thicknesses, blood content and water content are presented. The ratio of arterial and venous dermal blood was 1:1 [37]. Venous oxygen saturation was considered 10% lower than the arterial oxygen saturation [38]. An epidermal melanin concentration of 10% was considered in the model, approximating a medium-dark skin-complexion to represent the average skin-tone of the volunteers participated in the study [39]. The effect of skin hydration was

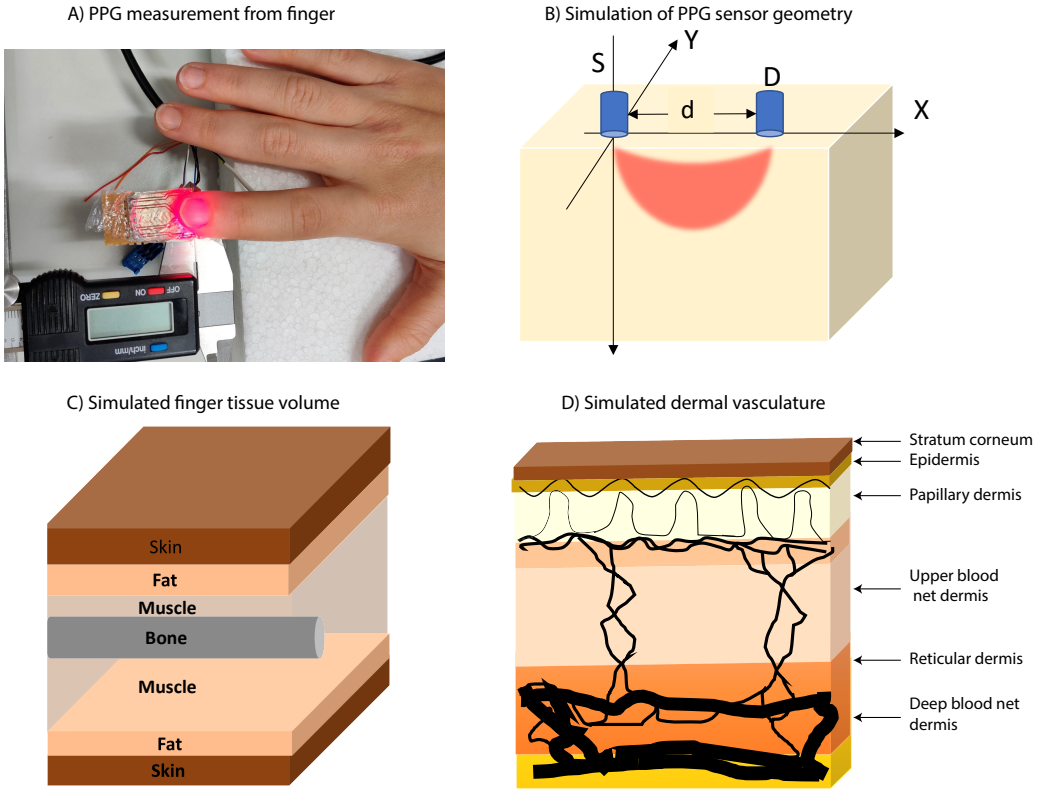

Figure 1. Shows the methodology of the current work. PPG signal was acquired from the index fingers of healthy volunteers using an in-house sensor prototype (A), and the underlying light-tissue interaction was explained using a Monte Carlo model. The 3D geometry of the model is presented in the Cartesian coordinate system (B) where X, Y and Z axes present the length, width and depth of the tissue. Simulated light source S and detector D are placed a distance 'd' apart on the tissue surface $z = 0$ where d is variable (between 1-10 mm). The red patch presents the characteristic optical path through the tissue volume probed by the sensor (typical banana-shaped path is seen in a homogeneous medium [2]). Details of the heterogeneous tissue-structure used in the model are presented in (C). Finger tissue volume has six layers; and a depth and width of 13 mm each, and a semi-infinite length. Simulated skin sublayers are presented in (D). The epidermis thicknesses is scaled down to illustrate the dermal vasculature at different depths. The yellow bottom layer represents subdermal tissue.

also taken into consideration. Parameters used to simulate the dermal sublayers, i.e., the thickness (t), blood volume (V_b) and volume of water in the dermal sublayers (V_w) are illustrated in Table 1.

2.1.2. Tissue optical properties The Monte Carlo model was optically characterised by the wavelength-dependent parameters: absorption coefficient (μ_a), scattering coefficient (μ_s), and scattering anisotropy (g). The optical properties were determined based on the hypothesis of the 'blood volume variations' [12]. In this volumetric approach, the cumulative absorption coefficient of the main absorbers was calculated, for example, blood chromophores (oxyhaemoglobin and deoxyhaemoglobin), water, melanin etc.

Table 1. Dermal sublayers: thickness (t), blood volume (V_b) and water volume (V_w). Parameters are adopted from the references [22,30,34,37,40,41].

Dermal Sublayer	t (mm)	V_b (%)	V_w (%)
stratum corneum	0.02	0	5
epidermis	0.25	0	20
papillary dermis	0.1	4	50
upper blood net dermis	0.08	30	60
reticular dermis	0.2	4	70
deep blood net dermis	0.3	10	70

According to the hypothesis, in the model, a certain volume increases in the pulsatile tissue-component (e.g., blood) would be accompanied by an equivalent decrease in the non-pulsatile tissue component (e.g., bloodless tissue).

The baseline absorption coefficient $\mu_{a_{baseline}}$ (i.e., the absorption coefficient of the dermal sublayer due to its intrinsic absorption property only in absence of any other chromophore) at an operating wavelength λ is expressed by the equation below [42,43]:

$$\mu_{a_{baseline}}(\lambda) = 7.84 \times 10^7 \times \lambda^{-3.255}. \tag{2}$$

Considering the absorbance of light through arterial and venous blood with different concentrations of oxyhaemoglobin (HbO_2) and deoxyhaemoglobin (HHb), the total absorption coefficient of any i^{th} dermal sublayer can be written as: [34,35,44]

$$\begin{aligned}\mu_{a_i}(\lambda) = V_{A_i}\mu_{a_{A_i}}(\lambda) + V_{V_i}\mu_{a_{V_i}}(\lambda) + V_{w_i}\mu_{a_{w_i}}(\lambda) \\ +[1-(V_{A_i}+V_{V_i}+V_{w_i})]\mu_{a_{baseline_i}}(\lambda)\end{aligned} \tag{3}$$

where V_A and V_V stand for the arterial and venous blood volume-fraction respectively. μ_{a_A}, μ_{a_V} and μ_{a_w} are the absorption coefficients of the arterial blood, venous blood and water. Oxygen saturation, by definition, is the concentration of oxygen saturated haemoglobin in the total blood. Considering SaO_2 and SvO_2 are respectively the functional arterial and venous oxygen saturation, absorption coefficients of the arterial and venous blood can be written as:

$$\begin{aligned}\mu_{a_A}(\lambda) &= SaO_2\mu_{a_{HbO_2}}(\lambda) + (1-SaO_2)\mu_{a_{HHb}}(\lambda) \\ \mu_{a_V}(\lambda) &= SvO_2\mu_{a_{HbO_2}}(\lambda) + (1-SvO_2)\mu_{a_{HHb}}(\lambda)\end{aligned} \tag{4}$$

where $\mu_{a_{HbO_2}}$ and $\mu_{a_{HHb}}$ are the absorption coefficients of oxy and deoxyhaemoglobin, respectively.

The epidermal layer of the skin is bloodless, and contains melanin and water. The melanin absorption coefficient $\mu_{a_{mel}}$ is determined from the following equation [41,45]:

$$\mu_{a_{mel}}(\lambda) = 6.6 \times 10^{10} \times \lambda^{-3.33} \tag{5}$$

which is used to derive the absorption coefficient for epidermis:

$$\mu_{a_{epi}}(\lambda) = V_{mel}\mu_{a_{mel}}(\lambda) + V_{w_{epi}}\mu_{a_w}(\lambda) + [1-(V_{mel}+V_{w_{epi}})]\mu_{a_{baseline}}(\lambda). \tag{6}$$

The absorption coefficients of water, oxyhaemoglobin and deoxyhaemoglobin (at a haematocrit of 45%) were adapted from literature [46–49]. The absorption coefficients of subdermal fat and muscle were adapted from the published data measured from

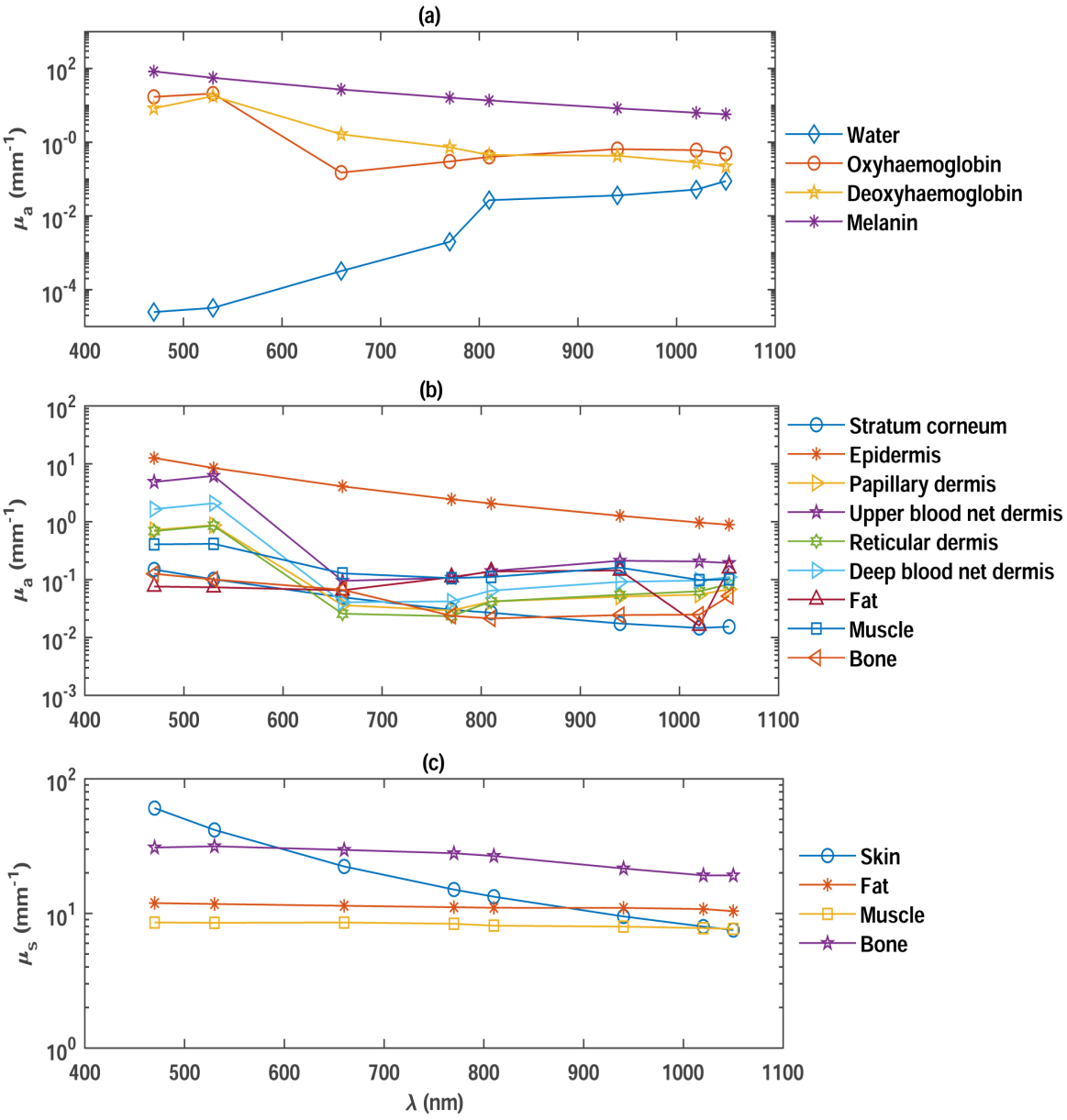

Figure 2. Optical properties of the tissue at the eight wavelengths: 470 nm, 530 nm, 660 nm, 770 nm, 810 nm, 940 nm, 1020 nm and 1050 nm. The absorption coefficient of the absorbers of the model (water, oxyhaemoglobin, deoxyhaemoglobin and melanin) are presented in (a). The absorption coefficients of the dermal skin sublayers (i.e., stratum corneum, epidermis papillary dermis, upper blood net dermis, reticular dermis and deep blood net dermis), fat, muscle and bone are presented in (b). The scattering coefficient of skin, fat, muscle and bone tissue layers are presented in (c). The coefficients are presented in the unit of mm^{-1} and in logarithmic scale. Details of the parameter values are given in the Appendix.

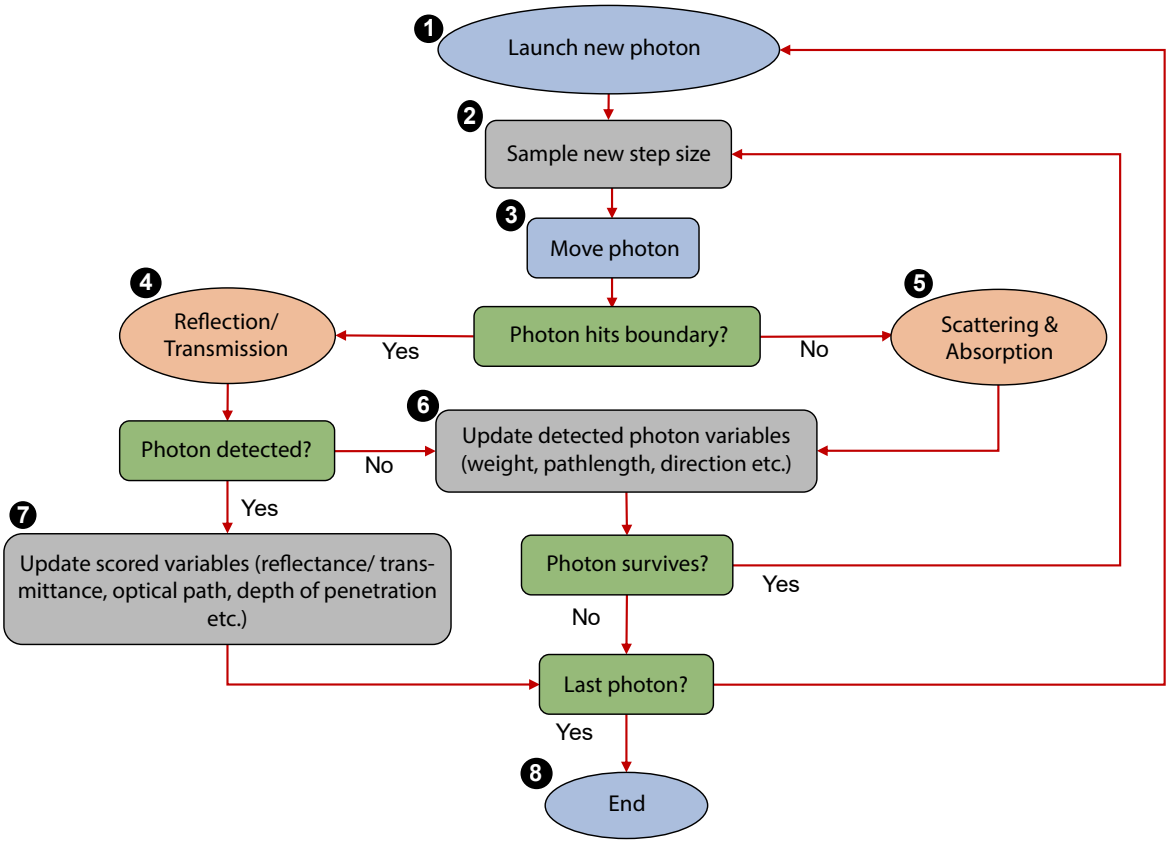

Figure 3. Flowchart of Monte Carlo algorithm.

human skin *ex vivo* [50]. Due to a lack of data on the optical properties of a finger bone, the optical properties of skull were used for the simulation [51,52]. The scattering coefficient and anisotropy factor of skin, muscle and bone were adapted from published studies [50,51,53–55]. The refractive indices for the tissue and air ($n_i = 1.4$ and $n_t = 1$, respectively) were considered in the model. The following optical properties used in the simulation at the eight wavelengths are illustrated in Figure 2: (a) absorption coefficients of the chromophores (i.e., oxyhaemoglobin, deoxyhaemoglobin, water and melanin), (b) the absorption and scattering coefficients of the tissue layers (skin, fat, muscle and bone) and (c) the skin sublayers (stratum corneum, epidermis, upper blood net dermis, papillary dermis, reticular dermis and deep blood net dermis). The values of the simulated parameters are tabulated in the Appendix.

2.1.3. Monte Carlo simulation A flowchart for the basic steps of the Monte Carlo (MC) simulation for the propagation of light through tissue in a finger-PPG configuration is presented in Figure 3. The simulation steps are as follows [56]:

(i) **Step 1:** A photon packet with an initial direction and position co-ordinate was launched onto the tissue surface. Similar to the incidence from an LED source, a

Gaussian beam incidence was simulated using the probability distribution:

$$p(r) = \frac{e^{\frac{-r^2}{b^2}} 2\pi r}{\pi b^2} \tag{7}$$

where b is the $1/e^2$ radius (i.e., the radius where the intensity values fall to $1/e^2$ of its axial values). The initial direction was randomly chosen between 0 and 2π, and an initial statistical weight $w = 1$ was allocated to each photon. A normal incidence of photons was considered and the correction due to the reflection from the top surface of the tissue was implemented. The Fresnel's reflection coefficient R_s for the normal incidence was calculated as [57, 58]:

$$R_s = \left(\frac{n_i - n_t}{n_i + n_t}\right)^2. \tag{8}$$

and the weight w of the photon was reduced by $R_s \cdot w$, resulting in a weight of the photon entering the tissue $w_e = w - R_s \cdot w$.

(ii) **Steps 2 and 3:** The photon packet was propagated through a step-size (l), calculated by random sampling of the probability of photon scatter [56], i.e.,

$$l = -\frac{ln(\xi)}{\mu_s} \tag{9}$$

where ξ is a computer-generated pseudo-random number ($0 < \xi < l$). The corresponding direction cosines of the photons were updated so that the movement of the photon could be simulated.

(iii) **Steps 4-7:** Upon each step size, i.e., free pathlength of the photon in the medium, it was checked whether the photon had interacted with the boundary. If a photon packet hit the boundary, it could either reflect back or transmit through the tissue. It was decided by calculating the Fresnel's reflectance R for the angle of incidence θ_i (critical angle, θ_C) following the equations below:

$$R = \begin{cases} \left(\frac{n_t - n_i}{n_i + n_t}\right)^2, & \text{if } \theta_i \simeq 0 \\ \frac{1}{2}\left[\frac{\sin^2(\theta_i - \theta_t)}{\sin^2(\theta_i + \theta_t)} + \frac{\tan^2(\theta_i - \theta_t)}{\tan^2(\theta_i + \theta_t)}\right], & \text{if } 0 < \theta_i < \theta_c \\ 1, & \text{if } \theta_c \leq \theta_i < \pi/2. \end{cases} \tag{10}$$

and comparing R with a randomly generated number ξ. On the other hand, if the photon propagated freely without hitting with the boundary, the photon-tissue interactions (i.e., absorption and scattering) were simulated. The 'absorption' was simulated by reducing a fraction of the photon weight (Δw) in each interaction:

$$\Delta w = \frac{\mu_a}{\mu_a + \mu_s}.w \tag{11}$$

The 'scattering' was simulated by orienting the direction of the photon packet through the randomly generated deflection and azimuthal angles. The scattering

angle θ was calculated using the Henyey-Greenstein phase function [59] whereas the azimuth was randomly generated between 0 and 2π:

$$\theta = \cos^{-1}\frac{1}{2g}\left[1+g^2-\left(\frac{1-g^2}{1-g+2g\xi}\right)^2\right] \qquad (12)$$
$$\phi = 2\pi\xi.$$

Upon each photon-tissue interaction event, i.e., reflection, transmission, scattering and absorption, the corresponding variables were recorded and updated.

(iv) **Step 8:** Above steps were repeated until the photon packet was either 'detected', 'discarded' or 'terminated'. The photon was discarded if it had transmitted without being detected. While travelling through tissue, if the weight of the photon fell below a threshold weight ($w < w_{th};\ w_{th} = 10^{-4}$), the Russian roulette technique was used to terminate the photon maintaining the energy conservation principle: one out of ten photons would get a chance to survive with an additional weight ($w' = 10.w$) and continue propagating. Photon not surviving roulette would be terminated and a new photon packet would launch. The process repeated until the desired number of photon packets were detected.

2.1.4. Model implementation The schematic of the Monte Carlo model in the reflectance PPG geometry is illustrated in Figure 1. In the 3D Cartesian coordinate system, the length, width and depth of the finger tissue volume are presented along the X, Y and Z (downward) axes, respectively. The most probable optical path is shown from the source to the detector through the tissue sample volume probed by the sensor. The typical 'banana' shaped path is shown, however, the path depends on the heterogeneity of the medium.

The key parameters simulated using the model are:

(i) **Mean depth of penetration (D_M)**: Penetration depth D of each i^{th} photon packet is calculated as its maximum z-coordinate (Z) while travelling from the source to the detector:

$$D_i = max(Z). \qquad (13)$$

The mean penetration depth (D_M) is calculated as the average maximum depth of all detected photons (i.e., N_d) at the particular source-detector separation d at a certain wavelength:

$$D_M = \frac{1}{N_d}\sum_{i=1}^{N_d} D_i \qquad (14)$$

(ii) **Absorbance (W_A)**: Absorbance in any layer or sublayer was calculated by the mean weight of the photon packet 'absorbed' in the medium. As shown in Eq. 15, a Δw fraction of each photon packet weight is absorbed in the medium at each interaction event. Considering an i^{th} photon packet interacts N times with a j^{th}

layer (or sublayer), the absorbance in that layer (or sublayer) is:

$$W_{A_j} = \frac{1}{N_{dl_j}} \sum_{i=1}^{N_{dl_j}} N \cdot \Delta w_j \tag{15}$$

where N_{dl_j} is the number of the detected photon packets that pass through the j^{th} layer or sublayer. For further analysis, the layer-specific absorbance is normalised by the total absorbance in the finger W_{A_T}, i.e.,

$$W_{A_T} = \frac{1}{N_d} \sum_{i=1}^{N_d} w_{e_i} - w_{d_i} \tag{16}$$

where w_{e_i} and w_{d_i} are the weight of the entered and detected photon packet, respectively. Therefore, the normalised layer-specific absorbance is:

$$W_{A_{j_{norm}}} = \frac{W_{A_j}}{W_{A_T}} \tag{17}$$

(iii) **Reflectance** (W_r): The mean detected weight of the photons in the PPG geometry is denoted by the term 'reflectance' W_r:

$$W_r = \frac{1}{N_d} \sum_{i=1}^{N_d} w_{d_i} \tag{18}$$

where N_d and w_d respectively are the total number of detected photon packets and the weight of each detected photon packet.

All the parameters are variable with the source-detector separation (d) and the operating wavelength (λ). A large number of photons ($10^9 - 10^{10}$) were simulated in order to obtain the desired accuracy. To expedite the process, the variance reduction technique was adopted in the model as described before. A 64-bit Operating System with an installed memory of 24 GB and an Intel Xeon CPU (2.40 GHz, 2 processors) was dedicated for the simulation. MATLAB (Mathworks, Inc., USA) platform was chosen for coding and a multi-thread programming environment was used for facilitating the simulation.

2.2. In vivo experimental setting and protocol

For the *in vivo* data collection, two reflectance PPG sensors each containing four LEDs were manufactured with the adjustable separation distance between the LEDs and the photo-diode. The first sensor consisted of 470 nm, 530 nm, 660 nm and 770 nm LEDs. The second sensor consisted of 810 nm, 940 nm 1020 nm and 1050 nm LEDs. The photodiode used was a wide bandwidth photodiode (*SFH 2700, Osram opto semiconductors*). The separation distance between emitter and photodiode was adjusted by attaching the PCBs containing the LEDs and the photodiode closely on the jaws of a vernier calliper. The minimum centre-to-centre distance between the LED and

photodiode when the calliper was at 0 mm was approximately 2 mm. The sensor was integrated with ZenPPG, a modular multi-channel PPG processing system developed by the Research Centre for Biomedical Engineering (RCBE) at City, University of London, to acquire multi-wavelength PPGs [60].

Following Institutional research ethics approval, healthy volunteers were invited to participate in the *in vivo* study. Eight healthy volunteers (5 male and 3 female) with age ranging from 20 to 35 years were recruited for this pilot study. The experiment took place in the Physiological Measurement laboratory of the RCBE, at City, University of London, under a constant room temperature of 23°C. Prior to the study, the thickness of each volunteer's finger was measured (the average finger thickness was 1.3 ± 1.1 cm). During the study, the volunteers were asked to sit steadily and to rest their arm on a table and then place their right index fingers on top of the reflectance sensor. PPG signals at four wavelengths were first collected simultaneously (using probe 1) throughout the source-detector separations from 1 mm to 10 mm with an interval of 1 mm. Each measurement continued for 1 minute and a 20 seconds interval was given between two consecutive measurements for the signals to stabilise. The above step was repeated using the second PPG sensor containing the other four LEDs. Recorded signals were analysed using MATLAB. The ac and dc components of the mixed-signal were extracted using the high pass and low pass filters, and the peak to peak amplitude was calculated for each signal (PPG_{ac} and PPG_{dc}, respectively). The signals were normalised over time.

2.3. Correlation analysis

In order to compare and correlate the simulated and experimental data, the absorbance and amplitudes ratios were calculated. The simulated absorbance ratio r_{sim} was calculated as the ratio between the normalised absorbance in the pulsatile tissue (dermis), i.e., W_{A_p} and non-pulsatile tissue (stratum corneum, epidermis, fat, muscle and bone), i.e., $W_{A_{np}}$:

$$r_{sim} = \frac{W_{A_{pnorm}}}{W_{A_{npnorm}}} \tag{19}$$

and the simulated PPG amplitude ratio r_{PPG} was defined as the ratio between the normalised ac and dc PPG amplitudes:

$$r_{PPG} = \frac{PPG_{ac}}{PPG_{dc}} \tag{20}$$

The correlation between the simulated and experimental data was presented in terms of the Pearson's Product Moment Correlation Coefficient which was derived using an in-built MATLAB function [61]. A paired data set $[(x_1, y_1), ...(x_k, y_k)]$, consisting of k such pairs, is considered. The mean of the individual data sets are:

$$\bar{x} = \frac{1}{k} \sum_{i=1}^{k} x_i \tag{21}$$

and

$$\bar{y} = \frac{1}{k}\sum_{i=1}^{k} y_i \tag{22}$$

where k is the length of the data set and i is the index of a data point. Therefore, the Pearson's Product Moment Correlation Coefficient $\rho(x, y)$ is defined as:

$$\rho(x,y) = \frac{\sum_{i=1}^{k}(x_i - \bar{x})(y_i - \bar{y})}{\sqrt{\sum_{i=1}^{k}(x_i - \bar{x})^2}\sqrt{\sum_{i=1}^{k}(y_i - \bar{y})^2}} \tag{23}$$

$\rho(x, y)$ can range between –1 to +1. A value of –1 indicates that one data set is the reverse of the other (negative correlation), while a value of +1 indicates that the data sets are the same (positive correlation). A value of 0 indicates no relationship between the data sets.

3. Results

3.1. PPG light-tissue interactions at multiple wavelengths and geometries

According to the modified Beer-Lambert law, as stated before, the trajectories of the photons through the tissue depend on the geometrical configuration and the optical wavelength. Typical photon trajectories within the skin tissue without any geometrical restriction are shown in Figure 4. Photon packets emerging from a point source placed at the origin of the 3D Cartesian co-ordinate system (0,0,0) travel through random paths in any direction within 2π until those are absorbed completely.

Optical interaction with the finger tissue-volume in a reflectance PPG geometry is shown in Figure 5. The distributions of the light-tissue interaction are shown for three source-detector separation distances (i.e., 1.5 mm, 3 mm and 5 mm) at four wavelengths (530 nm, 660 nm, 940 nm and 1050 nm). The tissue-depth is presented along the z-axis whilst the tissue-length is presented along the x-axis. As shown, the photon trajectories do not necessarily take the banana-shaped path which attributes to the heterogeneity of the model. The variations in the trajectories of the photons with different wavelengths and source-detector separations are apparent in the figure. At 530 nm, where light is highly absorbed by the blood, very few photons are detected especially at $d = 5$ mm. Photons paths become gradually longer within the tissue until 940 nm, and then the paths shorten again. The variations in the optical path is a result of the wavelength-dependent scattering properties of tissue. Maximum photons accumulate near the source and the detector; the highest photon number density is found within 1.5 mm due to the interactions with the dermal vasculature. The dashed line presents the mean penetration depth (D_M) of the photon packets which increases with the source-detector separation at all wavelengths except at 530 nm where it remains constant. In the PPG reflectance geometries, although the maximum depth traversed by the detected photon packets are long ($\simeq$ 6 mm), the mean depth is much smaller ($\leq$ 3 mm). This points towards the observation by R. Savo *et. al.* that the photon paths with smaller trajectories are more

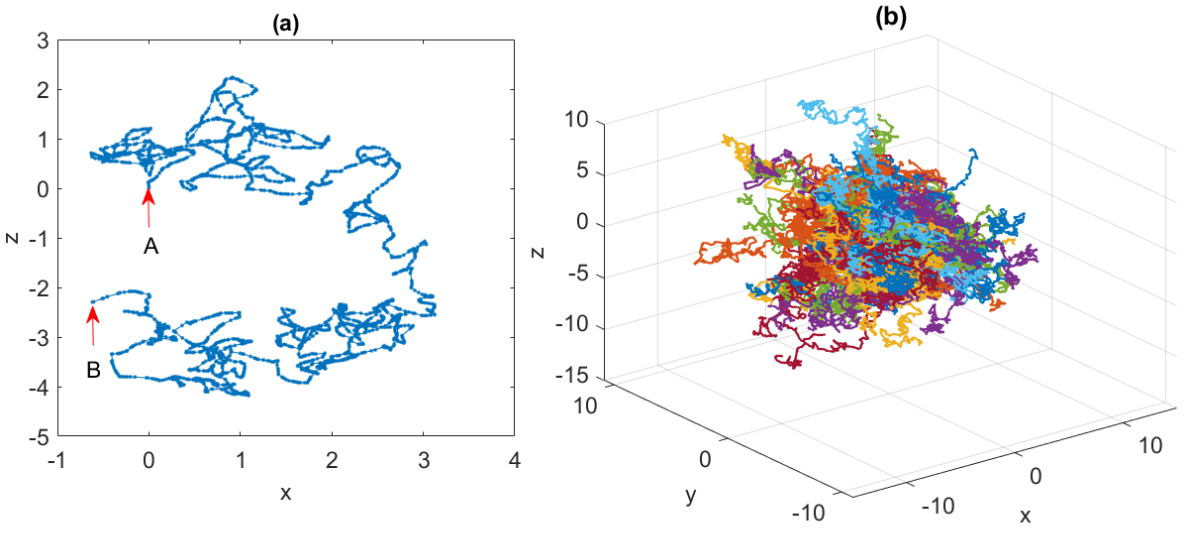

Figure 4. Monte Carlo simulation of photon trajectory through tissue. A typical path of a photon packet from a start-point A (0,0,0) to an end-point B in the skin tissue is presented in (a). Three-dimensional distribution of photon packets in the perfused skin tissue is presented in (b). The figures show the typical three-dimensional distribution of photon trajectories without any geometrical restriction at the wavelength of 660 nm. With no detector placement, the photons emerging from a point source placed at (0,0,0) are taking random free paths in all 2π dimensions.

probable compared to the longer trajectories [62]. Therefore, the mean penetration depth is considered as the characteristic depth probed by the sensor in this simulation.

Simulated results are supported by the PPG signal recorded *in vivo* as shown in Figures 6 and 7. In Figure 6, the signals recorded at the wavelength of 810 nm through various source-detector separations are exhibited, whereas in Figure 7, the signals recorded at multiple wavelengths at a source-detector separation of 2 mm are illustrated. The signal amplitude is found to reduce gradually with the increasing source-detector separation. With the increasing wavelength, the signal amplitudes initially rise reaching a maximum at the near-infrared wavelength of 940 nm, and then gradually reduce to the infrared wavelengths. The observations from the experimental results are in good agreement with the simulation outcome.

3.2. Depth-selective analysis of PPG amplitude

It is understood from the previous discussion that D_M is the characteristic depth to be probed by a PPG sensor in certain reflectance geometry. Also, as defined earlier, the reflectance W_r is a measure of the optical output from the sensor. A relationship between these two parameters is therefore investigated to correlate the optical outcome with the probed depth. Further analysis is carried out to correlate the simulated optical output and the measured PPG amplitudes.

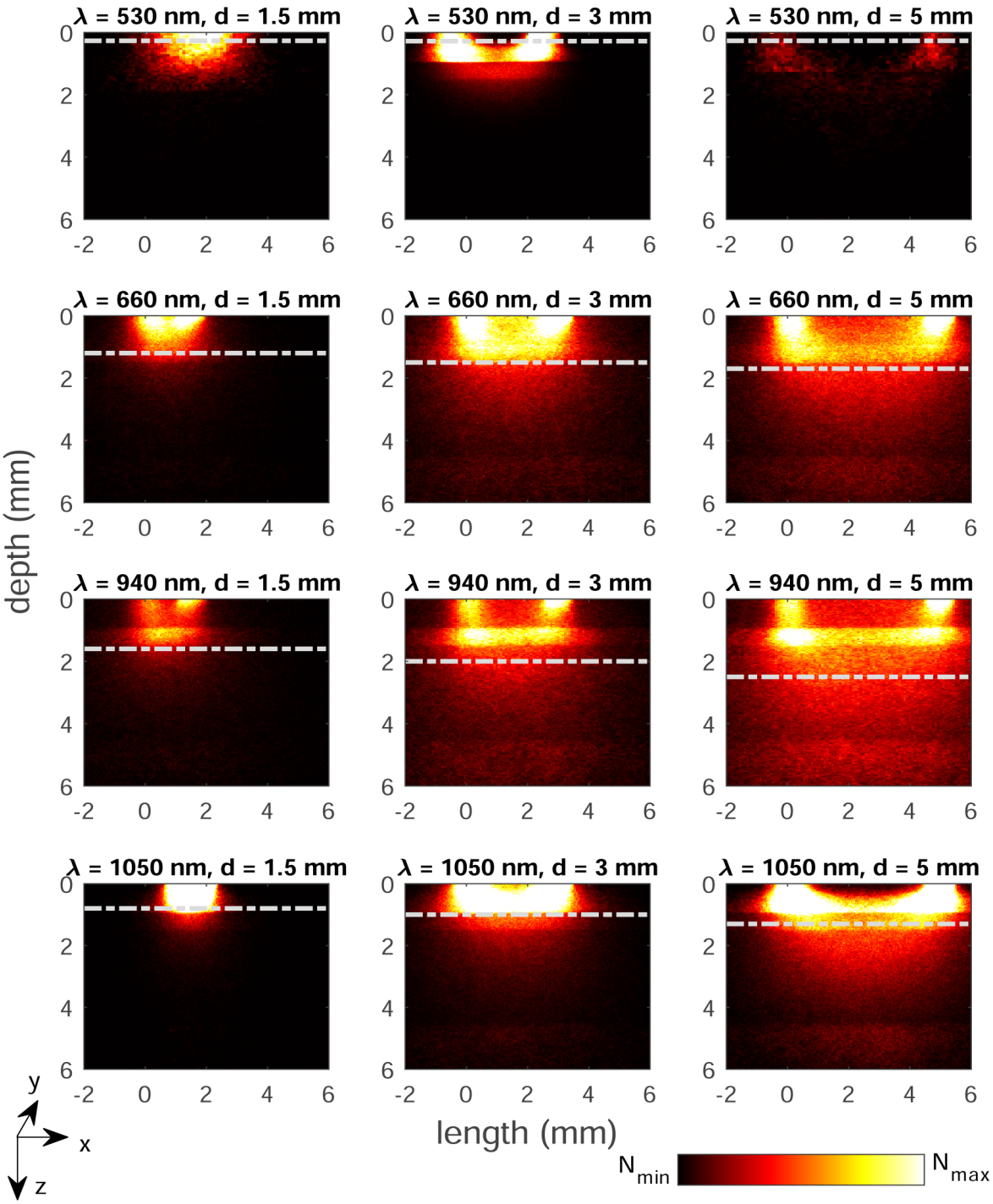

Figure 5. Simulated trajectories of the detected photons through tissue in PPG sensor geometry. Distributions are presented at four wavelengths (λ = 530 nm, 660 nm, 940 nm and 1050 nm) at three separation distances (d = 1.5 mm, 3 mm and 5 mm). The interaction events are distributed between its minimum and maximum values (N_{min} and N_{max}, respectively) as indicated by the colour bar. Photons distribution along with the depth and the length of the finger are shown through the z- and x-axis. The mean penetration depth (D_M) is presented by the white dashed line. All plots are presented in the same axis limits.

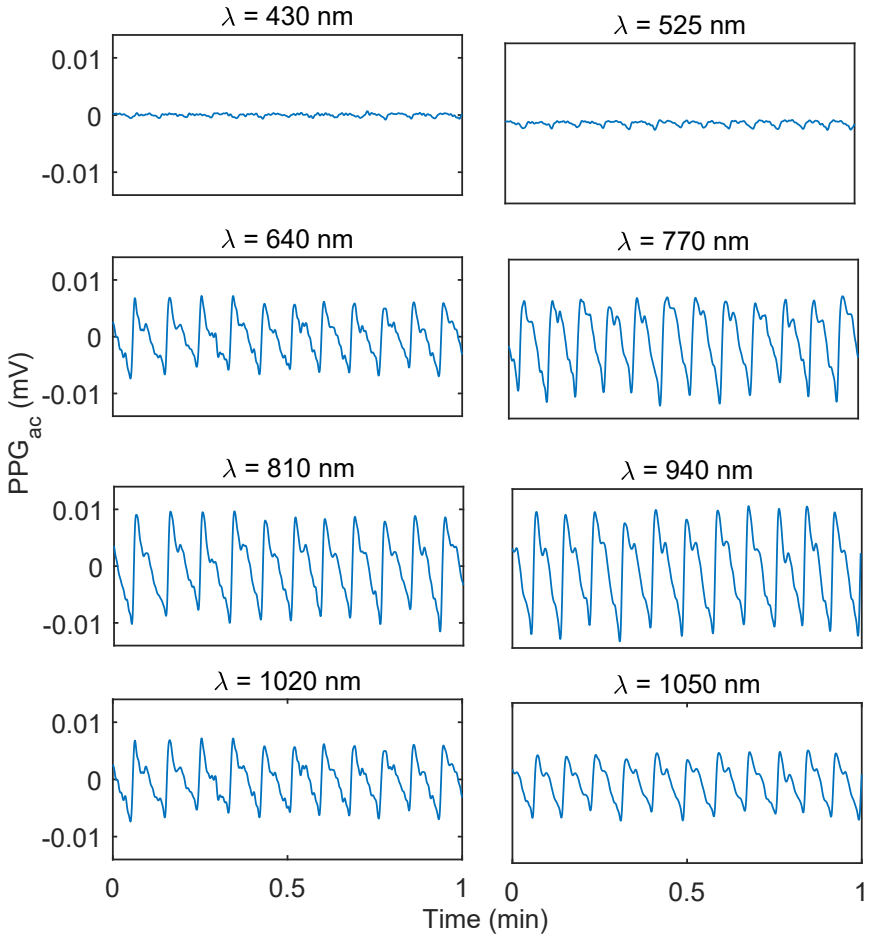

Figure 6. Demonstration of multiwavelength PPG (ac) signals recorded *in vivo*. Signals are recorded at a fixed source-detector separation of 2 mm through the wavelengths 430 nm, 525 nm, 640 nm, 770 nm, 810 nm, 940 nm, 1020 nm and 1050 nm. It shows the variation of the PPG amplitude with the operating wavelength as a result of the variation in the photon paths as shown in Figure 5.

The simulated mean depths of penetration and the reflectances for multiple wavelengths and source-detector separations are plotted in Figures 8(a) and (b) respectively. At 470 nm and 530 nm, there is visibly no change in D_M and W_r through the source-detector separations. The penetrated depths are very shallow (remains within the epidermal layer), and the detected reflectance is also very small at these wavelengths. For the rest of the wavelengths, D_M increases as W_r decreases exponentially with the increasing source-detector separations. With the increasing wavelength, D_M increases till 940 nm and reduces at the further infrared wavelengths. A converse relationship is observed in the pattern of W_r. The mean ac and dc PPG amplitudes at each wavelength with varying source-detector separation are shown in Figures 8(c) and (d). PPG signals at 460 nm and 525 nm cannot be obtained beyond the source-detector separation of 4 mm. A very high PPG (ac) amplitude peak is observed at 530 nm at small source-detector separation. This is attributed to the very high scattering coefficients of blood

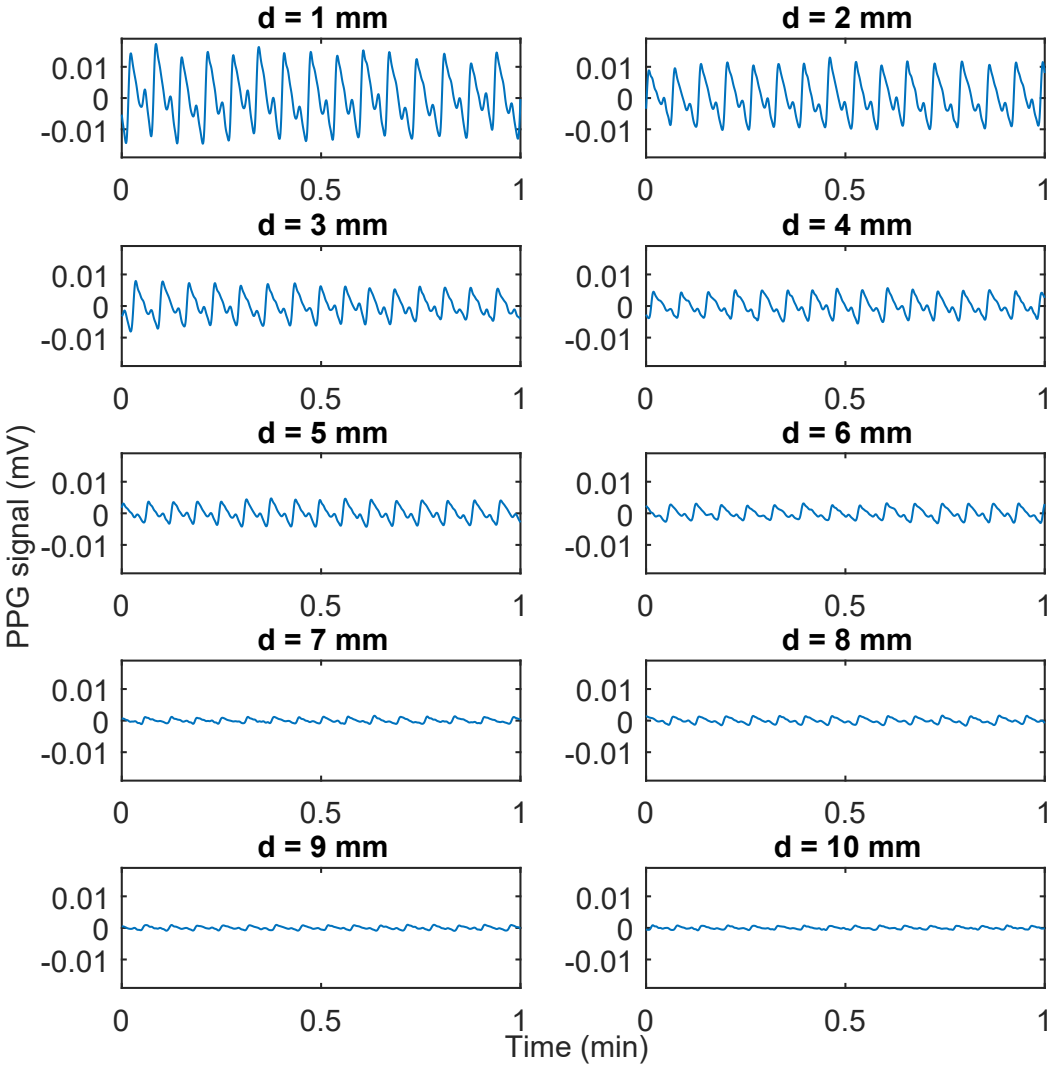

Figure 7. Demonstration of PPG (ac) signal recorded *in vivo* at the wavelength of 810 nm. Signals are recorded through the variable source-detector separations 1-10 mm. It shows the variation of the PPG amplitude with the source-detector separation as a result of the variation in the photon paths as shown in Figure 5.

(100 mm^{-1} and 92 mm^{-1}, respectively for the oxy and deoxyhaemoglobin) at 530 nm compared to the rest of the wavelengths [46]. The ac amplitude of PPG which is formed due to the pulsatile volumetric alterations in the blood is supposedly influenced by the scattering properties of blood because at 530 nm the probed volume is also low so the influence of other tissue-components is negligible.

3.3. Absorbance analysis and correlation assessment

Whilst the above result explained the qualitative interrelations between the optical output and the selected depths probed by the sensor, a quantitative analysis was carried out by investigating the absorbances at different depths, i.e., in different tissue layer and

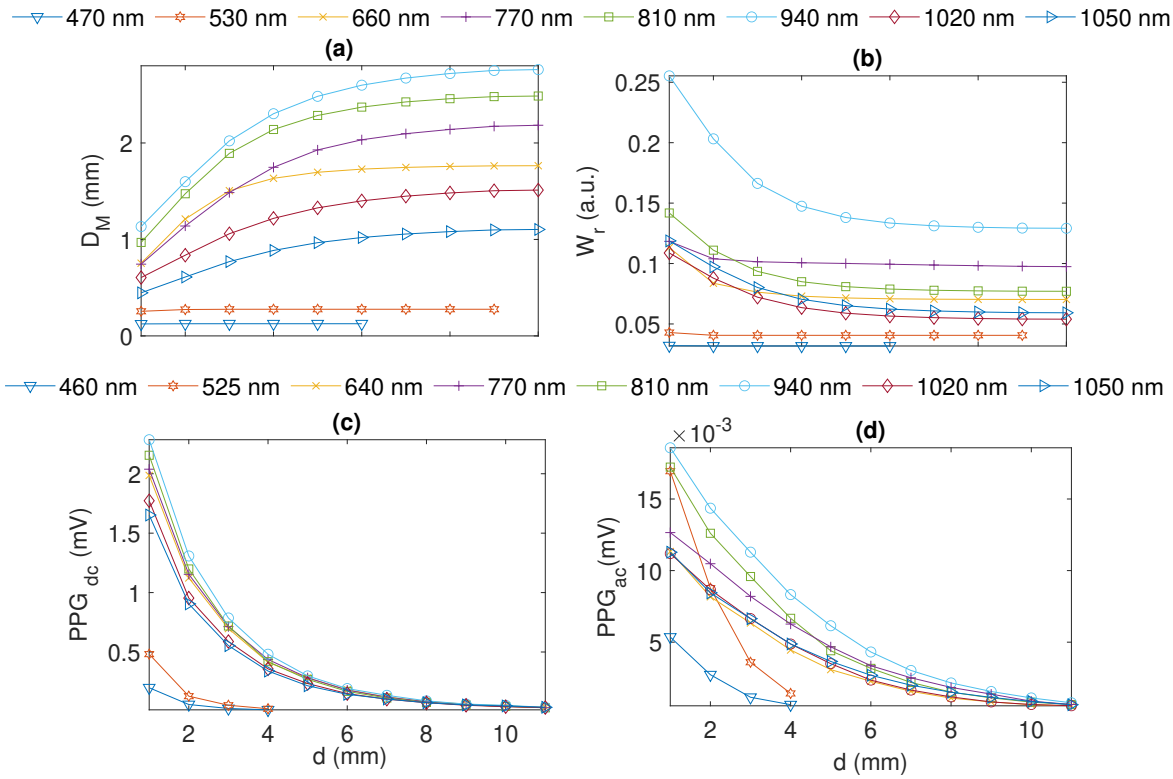

Figure 8. Illustration of the mean penetration depth D_M, simulated reflectance W_r and PPG amplitudes (ac and dc). With varying source-detector separation ($d = 1-10$ mm), the variations in D_M and W_r at eight wavelengths (λ) are presented in (a) and (b), and the variation in the PPG amplitude (dc and ac) are presented in (c) and (d), respectively. Markers show the data points. Absent data points at the two lowest wavelengths denote the unavailability of any data at higher separations.

sublayers. As defined by the Eq. 15, absorbance W_A in each tissue layer quantifies the mean absorbed photon weight within that layer which depends on the absorbed weight (Δw) and the number of interactions (N). Importantly, how many times a photon packet interacts with the tissue layer depends on the step size generated (Eq. 9) which is directly related to the scattering coefficient. Therefore, the layer-specific absorbance is a function of both the absorption and scattering coefficient of the tissue layer.

Simulated absorbance at the different tissue layers and sublayers at multiple source-detector separations and wavelengths are demonstrated in Figure 9. In the skin layers (stratum corneum, epidermis and dermis), the absorbance variation with the source-detector separation is negligible. Epidermis absorbs the maximum light due to the presence of melanin. Maximum light is absorbed in the dermis at 530 nm due to a high vascular absorptivity. Even though the blood absorptivity is higher at 470 nm, the number of photons reaching dermis at this wavelength is comparatively much lower resulting in the lowest absorbance. As observed in Figure 8, light penetrates the deepest through finger at 940 nm resulting in an increased number of interactions with the deeper tissue layer such as fat and muscle which explains the maximum absorbance of

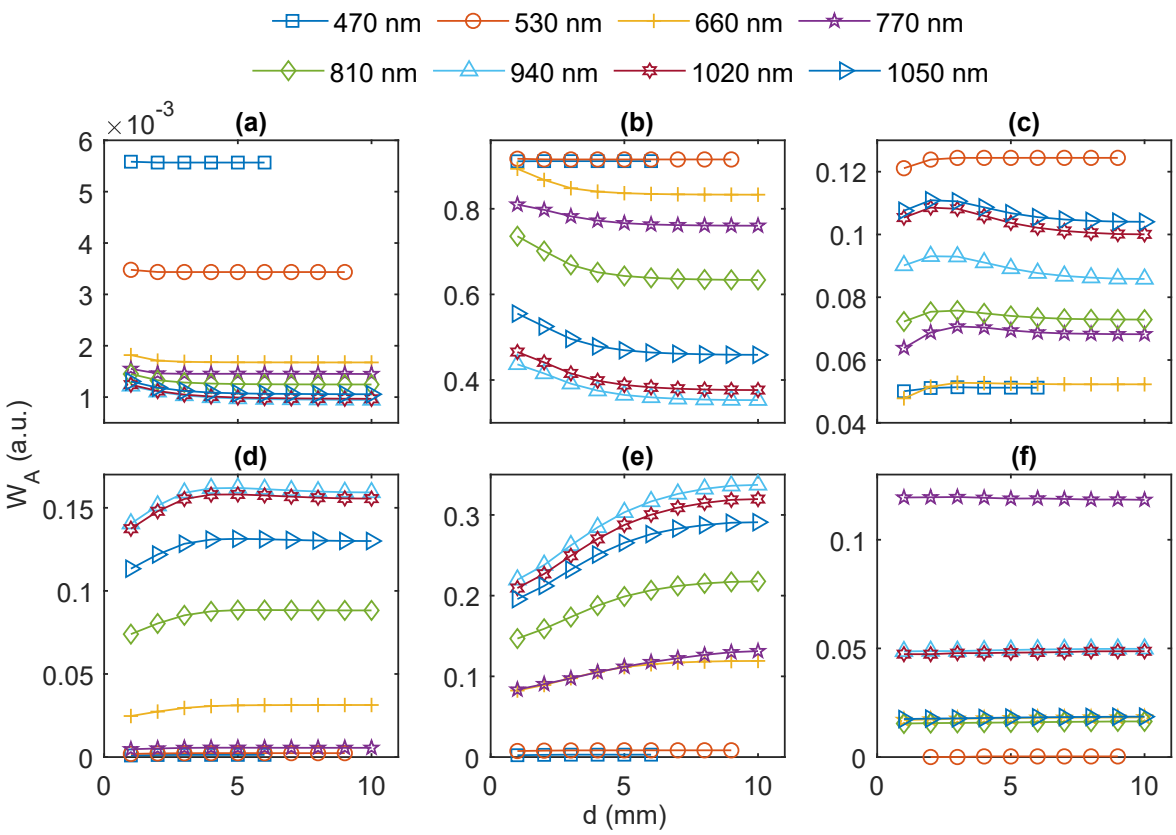

Figure 9. Simulated absorbance W_A through different tissue layer at 8 wavelengths as a function of the source-detector separation (d): (a) stratum corneum, (b) epidermis, (c) dermis, (d) fat, (e) muscle and (f) bone. The absorbance in the dermis is the sum of four dermal sublayer absorbances. Markers represent the data points. The absent data points at lower wavelengths denote the unavailability of data.

the optical wavelength at these two layers. Bone has the highest scattering coefficient among all tissue layers as seen in Figure 2, hence, the scattering effect prevails in the bone absorbance. Due to an increased scattering, a small number of photons that enter bone get detected resulting in a small $N_{d_{bone}}$ which in turn produces a high mean absorbance value. The maximum mean depth probed by the PPG sensor (D_M) is 3 mm as seen in Figure 8, i.e., well above the bone layer. Therefore, the impact of bone absorbance is negligible in PPG formation.

The simulated absorbance and experimental PPG amplitude ratios were calculated using Eq. 19 and 20, and were normalised against their respective maximum values, and then plotted in Figure 10 with a linear fit. All data points for eight wavelengths and ten source-detector separations are plotted. The absent data points (i.e., at higher separations at lower wavelengths) were considered zero in order to create the matrices of the same length. From Figure 10, the data shows a high correlation between the simulated and *in vivo* data with a negative slope of -0.86. To further quantify the correlations, the Pearson product-moment correlation coefficients (ρ) are calculated using Eq.23 and the results are presented in Table 2. The data sets x and y in the

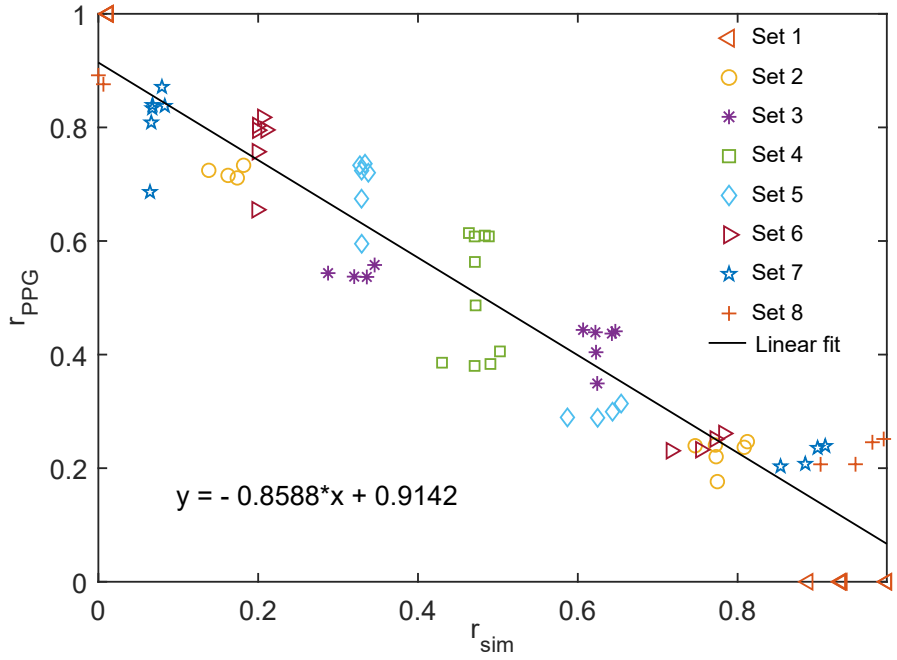

Figure 10. Relationship between the absorbance ratio r_{sim} and the PPG amplitude ratio r_{PPG} is shown. Eight sets of data represent the eight pairs wavelengths: (1) 470 nm (460 nm), (2) 530 nm (525 nm), (3) 660 nm, (4) 770 nm, (5) 810 nm, (6) 940 nm, (7) 1020 nm, and (8) 1050 nm. Data sets were normalised over their respective maximum values, thus distributed between 0 and 1. Each set of wavelengths have a ten number of data points corresponding to ten source-detector separations (1-10 mm). For the green and blue optical wavelengths, a couple of data points having adjacent values almost coincide in the graph, therefore, four data points at are visible for the set 1 and 2. Datasets are linearly fitted which produces a high negative slope.

Table 2. Pearson product-moment correlations ρ is presented for 10 source-detector separations (d). For each source-detector separation, the correlation coefficient has been determined between the spectra (arranged over eight wavelengths) of the simulated normalised absorbance and experimental PPG signals.

d (mm)	ρ
1	-0.94
2	-0.95
3	-0.94
4	-0.95
5	-0.98
6	-0.98
7	-0.96
8	-0.98
9	-0.96
10	-0.96

equation represent the spectra of r_{sim} and r_{PPG} over the eight operating wavelengths, and such 10 pairs of data sets are generated through the range of source-detector separation ($d = 1 - 10$ mm). For each data set, a very high negative correlation is found (average correlation coefficient -0.96) demonstrating an inverse relationship between the absorbance and PPG amplitudes.

4. Discussion

A robust Monte Carlo model for PPG has been developed and characterised in this paper. Monte Carlo method has been chosen over other methods for simulating light-tissue interactions, e.g., diffusion approximation, random walk model etc., because of its accuracy to model the photon distribution near and far from the source, and also the ability to recreate the random scattering within the tissue. The accuracy of the method can be quantified by its convergence rate, given by $1/\sqrt{Q}$ where Q is the number of simulations. The minimum number of simulated photon packet in this work was $Q = 10^9$ resulting in a very low convergence rate, i.e., 3.16×10^{-5} [63]. Lower the convergence rate, faster the stochastic process (i.e., Monte Carlo method) reaches the accuracy. Therefore, a high number of iterations produced a reliable and accurate result in this work.

Optical wavelength and geometrical configuration of the sensor are the two major factors affecting the optical quantities as well as the appearance of the PPG signal recorded by the system [2,64]. For the very first time, in this work, a Monte Carlo model has been explored to investigate the interrelations among (a) the optical quantities (e.g., depth of penetration, absorbance and reflectance); (b) the sensor parameters (geometry, source-detector separation and operating wavelength); and (c) the PPG signal parameters (ac and dc amplitudes). The dependence of the optical paths on the source-detector separation and wavelengths were illustrated through simulation, and was supported by the amplitude variation of the experimental PPG signals.

The exponential decay in the simulated reflectance as well as in the detected ac and dc PPG amplitudes has demonstrated the generic principle of light attenuation by Beer-Lambert law:

$$I = I_0 exp(-\mu.d) \tag{24}$$

where I and I_0 are the initial and final intensity of light while propagating through a tissue medium having attenuation coefficient μ; and d is the source-detector separation. Several interrelations have been observed through the simulations: a) an inverse relationship between the mean penetration depth and reflectance, b) a direct relationship between the PPG (dc) amplitude and the reflectance, (c) inverse relationships between the mean depth and the PPG (ac and dc) amplitudes, (d) a direct relationship between the depth and the source-detector separation, and (e) inverse relationship of the reflectance and the PPG amplitudes with the source-detector separations. Simulated results are immensely helpful for optimising the design of cutting-edge wearable sensors based on PPG technology.

Our previous work with a pulsatile PPG model showed the highest contribution of dermis (including the arterial, venous and capillary blood) to the formation of a PPG signal [23]. Based on this previous finding, in this current static PPG model, the entire dermis (consisting of arteries, veins and capillaries) was considered the 'pulsatile' tissue compartment forming the 'ac' PPG amplitude, and the rest of the finger tissue was considered the 'non-pulsatile' tissue compartment contributing to the formation of the 'dc' PPG amplitude. Although capillaries do not pulsate, the mechanical movements of the bunch of capillaries present in the finger accumulate to generate a pulsatile flow, hence, contributing to the 'ac' PPG fluctuations [13]. Venous blood does not contribute to the pulsatility, therefore, an overestimation in the simulated ratio could be present. This was corrected by normalising data sets over its maximum value.

Simulated results have shown the confinement of the blue light within a maximum penetration depth of 0.2 mm, i.e., primarily within the stratum corneum layer up to a certain distance through the epidermis. The green light penetrated through a maximum depth of 0.3 mm from the periphery, i.e., just crossed the epidermal boundary which is 0.27 mm. At usual PPG source-detector separation ($d > 3\ mm$), the visible light (i.e., 660 nm and 770 nm) penetrates through all of the dermal sublayers up to the fat layer (1.5 mm), whereas the near-infrared light (i.e., 810 nm and 940 nm) penetrates maximum distance within the tissue, i.e., beyond the subdermal fat and muscle layers ($>$ 2.5 mm). Higher near-infrared wavelengths (i.e, 1020 nm and 1050 nm) again penetrate shallower distances which likely to be the result of the water absorbance dominance. These results explain the shape of the absorption spectra of human tissue as shown in [65].

The PPG signals obtained in the red and the near-infrared wavelengths originate from the pulsatile arterioles that branch from the upper blood net dermis, having a maximum density in the reticular dermis. This supports the standard convention of PPG origin, and also the blood volume variation hypothesis by Mocco *et al.* [12]. Blue and green light produce detectable PPG signals even though these do not reach the pulsatile arterioles. The observation of the highest ac PPG amplitude at 525 nm among all wavelengths implies the prevailing effect of the absorbance of the dermal vasculature over the scattering properties which agrees with the finding by Denis G. Lapitan *et. al.* using a Beer-Lambert law-based model [19]. The origin of green PPG seems to support the hypothesis by Kamshilin *et al.* that the PPG formation is due to the modulation of the blood volume in the capillary bed induced by the pulsatile transmural pressure of the arteries. However, as described by Kamshilin *et. al.* in [13, 14], if PPGs at these wavelengths originates only due to the mechanical compression of capillaries, then they should be inverted in comparison to simultaneously acquired red PPG signal (red light is modulated by blood volume changes in arteries). But this was not the case in our experiment, indicating the potential presence of other causes behind the PPG formation. On the other hand, blue light, with its very shallow depth of penetration, cannot interrogate a large volume of the capillary network. Therefore, unlike the green light, the transmural pressure-induced mechanical changes in the capillaries may not

suffice to produce a detectable PPG signal with the blue light. The hypothesis by Volkov *et. al.* on the erythrocyte movements can be useful to explain the blue PPG. The movement in the red blood cells is rapid and distinct in different capillaries and is capable of modulating the light intensity significantly, which is recorded as the PPG signal.

Through our investigation, we conclude that all three above hypotheses are valid in terms of explaining the PPG origin. A high amplitude PPG signal, for example, the near-infrared PPG signal is likely to originate from the contributions of all of the aforementioned factors, and our future goal is to be able to decompose the effects of all the contributors from the signal. In order to achieve this goal, a further complex model including the physical capillaries, arterioles and arteries will be developed. A parallel pulsatile tissue phantom will be designed for an *in vitro* experiment to evaluate the simulation. The successful implementation of the *in silico - in vitro* model followed by the mathematical optimisation and decomposition analysis will enable us to have a comprehensive knowledge on the origin of the PPG as well as its shape and features.

In a heterogeneous tissue-model, the dermal blood apparently concentrates within a small volume of blood vessel (occupying 1-20% of the dermis volume) that is represented by high blood volumes (4-30%) in individual dermal sublayers. This concept was proposed by Meglisnki and Matcher [66] which has been followed by several researchers for their Monte Carlo simulations and experimental applications [67–72]. The absorption coefficients calculated using those values are also in agreement with the properties derived using diffusion approximation by Bosschaart *et. al.* [73]. In the current work, the blood volume fractions have been adapted from the literature by Meglinski and Matcher. Considering a uniform distribution, however, the average dermal blood volume fraction is approximated as low as 0.2% which was described by Jacques [65], and has been considered for various Monte Carlo modelling applications [74–77]. The blood volume proposed by Megilinski and Matcher are significantly higher compared to the values used by Fredriksson *et. al.* for the laser Doppler flowmetry model [78]. A higher blood content may cause an overestimation of the absorbance at each wavelength, however, this will not majorly impact the relative changes between the PPG wavelengths. In this work, the correlations demonstrated between the simulated and experimental outcomes validated the model for the current application. Further investigations are imperative for an accurate estimation of the dermal blood content and developing a more robust PPG model.

5. Conclusion

A multilayer multiwavelength Monte Carlo model for finger-PPG has been explored for estimating the contributions of different tissue layers and sublayers in the formation of the signal. A set of *in vivo* experiments have been followed, and the results showed excellent agreement with the simulated data. The contributions of three different factors (i.e, the variation in arterial blood volume, the mechanical properties of capillaries and

the erythrocyte movement) in the formation of the PPG signal have been demonstrated. For the very first time, the correlation between the normalised absorbance and the PPG amplitudes has been rigorously evaluated. The present work contributes to the fundamental knowledge of PPG which is essential for the future development and advancement of this technique.

Appendix

The optical parameters presented in the Figure 2 are illustrated below which include the absorption coefficients μ_a of the absorbers and the tissue layers-sublayers, and the scattering coefficients μ_s and scattering anisotropy factor g of the tissue layers.

$\lambda\ (nm) - >$		**470**	**530**	**660**	**770**	**810**	**940**	**1020**	**1050**
$\mu_a\ (mm^{-1})$	water	2.47E-05	3.20E-05	0.00032	0.0019858	0.026737	0.036	0.052	0.0885
	oxyhaemoglobin	17.05	20.91	0.15	0.3	0.4	0.65	0.61	0.49
	deoxyhaemoglobin	8.29	17.82	1.64	0.73	0.45	0.43	0.28	0.22
	melanin	83.46	55.94	26.94	16.13	13.62	8.30	6.32	5.74
$\mu_a\ (mm^{-1})$	stratum corneum	0.149	0.101	0.049	0.030	0.023	0.017	0.014	0.014
	epidermis	12.62	8.46	4.07	2.44	2.07	1.26	0.97	0.89
	papillary dermis	0.719	0.873	0.036	0.029	0.042	0.051	0.055	0.068
	upper blood net dermis	4.87	6.19	0.09	0.11	0.14	0.21	0.20	0.19
	reticular dermis	0.688	0.852	0.026	0.023	0.042	0.055	0.063	0.083
	deep blood net dermis	1.65	2.08	0.040	0.042	0.064	0.091	0.097	0.110
	fat	0.076	0.073	0.065	0.110	0.138	0.144	0.016	0.157
	muscle	0.406	0.415	0.128	0.106	0.111	0.161	0.098	0.10
	bone	0.126	0.1004	0.0667	0.0237	0.0213	0.0244	0.0248	0.0518
$\mu_s\ (mm^{-1})$	skin	60.61	41.74	22.33	15.05	13.32	9.50	7.99	7.52
	fat	11.94	11.757	11.40	11.12	11.02	10.99	10.78	10.40
	muscle	8.57	8.52	8.56	8.38	8.11	7.98	7.78	7.67
	bone	30.88	31.54	29.66	28	26.71	21.57	19.18	19.18
g	skin	0.838	0.886	0.913	0.926	0.932	0.942	0.949	0.951
	fat	0.9	0.9	0.9	0.9	0.9	0.9	0.9	0.9
	muscle	0.7748	0.7949	0.8813	0.9013	0.9088	0.9112	0.9188	0.9187
	bone	0.93	0.93	0.93	0.93	0.93	0.93	0.93	0.93

References

[1] Budidha K. Kyriacou, P. A. and T. Y. Abay. Optical techniques for blood and tissue oxygenation. *Encyclopedia of Biomedical Engineering, ed R. Narayan (Oxford: Elsevier)*, pages 461–472, 2019.

[2] S. Chatterjee, J. P. Phillips, and P. A Kyriacou. Monte carlo investigation of the effect of blood volume and oxygen saturation on optical path in reflectance pulse oximetry. *Biomedical Physics & Engineering Express*, 2(6):065018, 2016.

[3] Susan DeMeulenaere. Pulse oximetry: uses and limitations. *The Journal for Nurse Practitioners*, 3(5):312–317, 2007.

[4] Louise A Jensen, Judee E Onyskiw, and NGN Prasad. Meta-analysis of arterial oxygen saturation monitoring by pulse oximetry in adults. *Heart & Lung: The Journal of Acute and Critical Care*, 27(6):387–408, 1998.

[5] M. Hickey, J. P. Phillips, and P. A. Kyriacou. Investigation of peripheral photoplethysmographic morphology changes induced during a hand-elevation study. *Journal of Clinical Monitoring and Computing*, 30(5):727–736, 2016.

[6] T. Y. Abay and P. A. Kyriacou. Reflectance photoplethysmography as noninvasive monitoring of tissue blood perfusion. *IEEE Trans. Biomed. Eng.*, 62(9):2187–2195, 2015.

[7] K. Budidha and P. A. Kyriacou. In vivo investigation of ear canal pulse oximetry during hypothermia. *J. Clin. Monit.*, pages 1–11, 2017.

[8] H. Njoum and P. A. Kyriacou. Photoplethysmography for an independent measure of pulsatile pressure under controlled flow conditions. *Physiol. Meas.*, 38(2):87, 2016.

[9] H. Njoum and P. A. Kyriacou. Photoplethysmography for the assessment of haemorheology. *Sci. Rep.*, 7(1):1406, 2017.

[10] Jing Liu, Bryan P Yan, Yuan-Ting Zhang, Xiao-Rong Ding, Peng Su, and Ni Zhao. Multi-wavelength photoplethysmography enabling continuous blood pressure measurement with compact wearable electronics. *IEEE Transactions on Biomedical Engineering*, 66(6):1514–1525, 2019.

[11] Jing Liu, Bryan Ping-Yen Yan, Wen-Xuan Dai, Xiao-Rong Ding, Yuan-Ting Zhang, and Ni Zhao. Multi-wavelength photoplethysmography method for skin arterial pulse extraction. *Biomedical optics express*, 7(10):4313–4326, 2016.

[12] Andreia V Moço, Sander Stuijk, and Gerard Haan. New insights into the origin of remote ppg signals in visible light and infrared. *Scientific Reports*, 8(1):8501, 2018.

[13] Alexei A Kamshilin and Nikita B Margaryants. Origin of photoplethysmographic waveform at green light. *Physics Procedia*, 86:72–80, 2017.

[14] Alexei A Kamshilin, Ervin Nippolainen, Igor S Sidorov, Petr V Vasilev, Nikolai P Erofeev, Natalia P Podolian, and Roman V Romashko. A new look at the essence of the imaging photoplethysmography. *Scientific reports*, 5:10494, 2015.

[15] Alexei A Kamshilin, Oleg V Mamontov, Vasily T Koval, Grigory A Zayats, and Roman V Romashko. Influence of a skin status on the light interaction with dermis. *Biomedical optics express*, 6(11):4326–4334, 2015.

[16] Meir Nitzan, Yair Adar, Ellie Hoffman, Eran Shalom, Shlomo Engelberg, Iddo Ben-Dov, and Michael Bursztyn. Comparison of systolic blood pressure values obtained by photoplethysmography and by korotkoff sounds. *Sensors*, 13(11):14797–14812, 2013.

[17] Takuo Aoyagi. Pulse oximetry: its invention, theory, and future. *Journal of anesthesia*, 17(4):259–266, 2003.

[18] Susan M Daly and Martin J Leahy. 'Go with the flow': a review of methods and advancements in blood flow imaging. *Journal of biophotonics*, 6(3):217–255, 2013.

[19] Denis G Lapitan and Andrey P Tarasov. Analytical assessment of the modulation depth of photoplethysmographic signal based on the modified Beer-Lambert law. In *2019 IEEE 8th International Conference on Advanced Optoelectronics and Lasers (CAOL)*, pages 103–106. IEEE, 2019.

[20] Mikhail V. Volkov, Nikita B. Margaryants, Andrey V. Potemkin, Maxim A. Volynsky, Igor P. Gurov, Oleg V. Mamontov, and Alexei A. Kamshilin. Video capillaroscopy clarifies mechanism of the photoplethysmographic waveform appearance. *Scientific Reports*, 7(1):13298.

[21] David T Delpy, Mark Cope, Pieter van der Zee, SR Arridge, Susan Wray, and JS Wyatt. Estimation of optical pathlength through tissue from direct time of flight measurement. *Physics in Medicine & Biology*, 33(12):1433, 1988.

[22] J. L. Reuss. Multilayer modeling of reflectance pulse oximetry. *IEEE Transactions on Biomedical Engineering*, 52(2):153–159, 2005.

[23] S. Chatterjee and P. A. Kyriacou. Monte carlo analysis of optical interactions in reflectance and transmittance finger photoplethysmography. *Sensors*, 19(4):789, 2019.

[24] A. Doronin, I. Fine, and I. Meglinski. Assessment of the calibration curve for transmittance pulse-oximetry. *Laser Phys.*, 21(11):1972–1977, 2011.

[25] A. Doronin. *The unified Monte Carlo model of photon migration in scattering tissue-like media for the needs of Biomedical Optics*. PhD thesis, University of Otago, New Zeeland, 2014.

[26] A. Doronin and I. Meglinski. Online object oriented Monte Carlo computational tool for the needs

of biomedical optics. *Biomed. Opt. Express*, 2(9):2461–2469, 2011.

[27] John A Gosling, Philip F Harris, John R Humpherson, Ian Whitmore, and Peter LT Willan. *Human Anatomy, Color Atlas and Textbook E-Book*. Elsevier Health Sciences, 2016.

[28] CE Garrido Varas and Tim JU Thompson. Metric dimensions of the proximal phalanges of the human hand and their relationship to side, position, and asymmetry. *Homo*, 62(2):126–143, 2011.

[29] Michael Darowish, Rodney Brenneman, and Justin Bigger. Dimensional analysis of the distal phalanx with consideration of distal interphalangeal joint arthrodesis using a headless compression screw. *Hand*, 10(1):100–104, 2015.

[30] Gray's Anatomy. The anatomical basis of clinical practice, 39th eds. *Am. J. Neuroradiol.*, 26(10):2703, 2005.

[31] Ying Yang, Asha Rupani, Pierre O Bagnaninchi, Ian Wimpenny, and Alan P Weightman. Study of optical properties and proteoglycan content of tendons by polarization sensitive optical coherence tomography. *Journal of biomedical optics*, 17(8):081417, 2012.

[32] Ali Shuaib. *Characterizing optical properties in fibrous tissues*. PhD thesis, University of Missouri–Columbia, 2011.

[33] V. V. Tuchin, A. N. Bashkatov, E. A. Genina, V. I. Kochubey, V. V. Lychagov, S. A. Portnov, N. A. Trunina, D. R. Miller, S. Cho, H. Oh, B. Shim, M. Kim, J. Oh, H. Eum, Y. Ku, D. Kim, and Y. Yang. Finger tissue model and blood perfused skin tissue phantom. volume 7898, page 78980Z. Proc. SPIE Dyn. Fluctuations Biomed. Photonics, 2011.

[34] V. V Tuchin. *Advanced biophotonics: tissue optical sectioning*. Taylor and Francis, CRC Press, USA, 2013.

[35] I. V. Meglinski and S. J. Matcher. Computer simulation of the skin reflectance spectra. *Comput. Methods Programs Biomed.*, 70(2):179–186, 2003.

[36] James G Marks and Jeffrey J Miller. *Lookingbill and Marks' Principles of Dermatology E-Book*. Elsevier Health Sciences, 2017.

[37] J. L. Reuss and D. Siker. The pulse in reflectance pulse oximetry: and experimental studies. *J. Clin. Monit. Comput.*, 18(4):289–299, 2004.

[38] Meir Nitzan and Haim Taitelbaum. The measurement of oxygen saturation in arterial and venous blood. *IEEE Instrumentation & Measurement Magazine*, 11(3):9–15.

[39] Josef Thingnes, Timothy J Lavelle, Eivind Hovig, and Stig W Omholt. Understanding the melanocyte distribution in human epidermis: an agent-based computational model approach. *PloS one*, 7(7), 2012.

[40] V. V Tuchin. Light scattering study of tissues. *Physics-Uspekhi*, 40(5):495–515, 1997.

[41] S. L. Jacques. Skin optics summary. 1998.

[42] I. S. Saidi. *Transcutaneous optical measurement of hyperbilirubinemia in neonates*. PhD thesis, Rice University, USA, 1992.

[43] S. L. Jacques. Origins of tissue optical properties in the UVA, visible, and NIR regions. *OSA TOPS Adv. Opt. imaging Phot. Migr.*, 2:364–369, 1996.

[44] J. M. Schmitt and "Schmitt. Simple photon diffusion analysis of the effects of multiple scattering on pulse oximetry. *IEEE Trans. Biomed. Eng.*, 38(12):1194–1203, 1991.

[45] S. L. Jacques and D. J. McAuliffe. The melanosome: threshold temperature for explosive vaporization and internal absorption coefficient during pulsed laser irradiation. *Photochem. Photobiol.*, 53(6):769–775, 1991.

[46] N. Bosschaart, G. J. Edelman, M. C. G. Aalders, T. G. Van Leeuwen, and D. J. Faber. A literature review and novel theoretical approach on the optical properties of whole blood. *Lasers Med. Sci.*, 29(2):453–479, 2014.

[47] J. Laufer, R. Simpson, M. Kohl, M. Essenpreis, and M. Cope. Effect of temperature on the optical properties of ex vivo human dermis and subdermis. *Phys. Med. Biol.*, 43:2479–2489, 1998.

[48] J. M. Steinke and A. P. Shepherd. Diffusion model of the optical absorbance of whole blood. *J. Opt. Soc. Am. A.*, 5(6):813–822, 1988.

[49] G. M. Hale and M. R. Querry. Optical constants of water in the 200-nm to 200-m wavelength region. *Appl. Opt.*, 12(3):555, March 1973.

[50] C. R. Simpson, M. Kohl, M. Essenpreis, and M. Cope. Near-infrared optical properties of ex vivo human skin and subcutaneous tissues measured using the monte carlo inversion technique. *Phys.Med.Biol.*, 43(9):2465–2478, 1998.

[51] A. N. Bashkatov, E. A. Genina, V. I. Kochubey, and V. V Tuchin. Optical properties of human cranial bone in the spectral range from 800 to 2000 nm. volume 6163, page 616310. Proceedings of SPIE, 2006.

[52] Michael Firbank. *The design, calibration and usage of a solid scattering and absorbing phantom for near infra red spectroscopy.* PhD thesis, University of London, 1994.

[53] AN Bashkatov, EA Genina, VI Kochubey, and VV Tuchin. Optical properties of the subcutaneous adipose tissue in the spectral range 400–2500 nm. *Optics and spectroscopy*, 99(5):836–842, 2005.

[54] Yong Du, XH Hu, M Cariveau, X Ma, GW Kalmus, and JQ Lu. Optical properties of porcine skin dermis between 900 nm and 1500 nm. *Physics in Medicine & Biology*, 46(1):167, 2001.

[55] V. I. Kochubey M. D. Kozintseva A. N. Bashkatov, E. A. Genina and V. V. Tuchin. Optical properties of muscle tissue. In S Solomon, D Qin, M Manning, Z Chen, M Marquis, K B Averyt, M Tignor, and H L Miler, editors, *Internet report, Saratov Fall Meeting*. 2011.

[56] L. Wang, S. L. Jacques, and L. Zheng. Mcml-Monte Carlo of light transport in multi-layered tissues. *Comput. Methods Programs*, 47(2):131–146, 1995.

[57] Max Born and Emil Wolf. *Principles of Optics: Electromagnetic Theory of Propagation, Interference and Diffraction of Light*. Elsevier, 2013.

[58] A. R. Ganesan and E. Hecht. *Optics*. Pearson Education, 2008.

[59] L. G. Henyey and J. L. Greenstein. Diffuse radiation in the galaxy. *Astrophys. J.*, 93:70–83, 1941.

[60] K. Budidha, V. Rybynok, and P. A. Kyriacou. Design and development of a modular, multichannel photoplethysmography system. *IEEE Transactions on Instrumentation and Measurement*, 67(8):1954–1965, 2018.

[61] D Rasch. Gibbons, jd: Nonparametric statistical inference, statistics: Textbooks and monographs vol. 65. marcel dekker, inc., new york and basel 1985. *Biometrical Journal*, 28(8):936–936, 1986.

[62] Romolo Savo, Romain Pierrat, Ulysse Najar, Rémi Carminati, Stefan Rotter, and Sylvain Gigan. Mean path length invariance in multiple light scattering. *arXiv:1703.07114*, 2017.

[63] Bernard Lapeyre, Étienne Pardoux, Etienne Pardoux, and Rémi Sentis. *Chapter 1 in Introduction to Monte Carlo methods for transport and diffusion equations*, volume 6. Oxford University Press on Demand, 2003.

[64] S. Chatterjee, T. Y. Abay, J. P. Phillips, and P. A. Kyriacou. Investigating optical path and differential pathlength factor in reflectance photoplethysmography for the assessment of perfusion. *Journal of biomedical optics*, 23(7):075005, 2018.

[65] Steven L Jacques. Optical properties of biological tissues: a review. *Physics in Medicine and Biology*, 58(11):R37–R61, 2013.

[66] I. V. Meglinski and S. J. Matcher. Quantitative assessment of skin layers absorption and skin reflectance spectra simulation in the visible and near-infrared spectral regions. *Physiological Measurement.*, 23(4):741–753, 2002.

[67] Alec B Walter, Jocelyn Simpson, J Logan Jenkins, Eric P Skaar, and E Duco Jansen. Optimization of optical parameters for improved photodynamic therapy of staphylococcus aureus using endogenous coproporphyrin iii. *Photodiagnosis and Photodynamic Therapy*, 29:101624, 2020.

[68] Tom Lister, Philip A Wright, and Paul H Chappell. Simulating light transport through skin for color prediction of port wine stain lesions: a review. *Journal of biomedical optics*, 17(11):110901, 2012.

[69] Takaaki Maeda, Naomi Arakawa, Motoji Takahashi, and Yoshihisa Aizu. Monte carlo simulation of spectral reflectance using a multilayered skin tissue model. *Optical review*, 17(3):223–229, 2010.

[70] Sonja Huclova, Daniel Erni, and Jürg Fröhlich. Modelling and validation of dielectric properties

of human skin in the mhz region focusing on skin layer morphology and material composition. *Journal of Physics D: Applied Physics*, 45(2):025301, 2011.

[71] Ethan PM LaRochelle, Kayla Marra, Robert E LeBlanc, M Shane Chapman, Edward V Maytin, and Brian W Pogue. Modeling ppix effective light fluence at depths into the skin for pdt dose comparison. *Photodiagnosis and photodynamic therapy*, 25:425–435, 2019.

[72] Yu Shimojo, Takahiro Nishimura, Hisanao Hazama, Toshiyuki Ozawa, and Kunio Awazu. Measurement of absorption and reduced scattering coefficients in asian human epidermis, dermis, and subcutaneous fat tissues in the 400-to 1100-nm wavelength range for optical penetration depth and energy deposition analysis. *Journal of Biomedical Optics*, 25(4):045002, 2020.

[73] Nienke Bosschaart, Rosaline Mentink, AGJM Ton van Leeuwen, Maurice CG Aalders, and Joke H Kok. Optical properties of neonatal skin measured in vivo as a function of age and skin pigmentation. *Journal of biomedical optics*, 16(9):097003, 2011.

[74] Steven L Jacques. Coupling 3d monte carlo light transport in optically heterogeneous tissues to photoacoustic signal generation. *Photoacoustics*, 2(4):137–142, 2014.

[75] AM Verga Scheggi, S Martellucci, Arthur N Chester, and R Pratesi. *Biomedical optical instrumentation and laser-assisted biotechnology*, volume 325. Springer Science & Business Media, 1996.

[76] Izumi Nishidate, Takaaki Maeda, Yoshihisa Aizu, and Kyuichi Niizeki. Visualizing depth and thickness of a local blood region in skin tissue using diffuse reflectance images. *Journal of Biomedical optics*, 12(5):054006, 2007.

[77] Tianhong Dai, Brian M Pikkula, Lihong V Wang, and Bahman Anvari. Comparison of human skin opto-thermal response to near-infrared and visible laser irradiations: a theoretical investigation. *Physics in Medicine & Biology*, 49(21):4861, 2004.

[78] Ingemar Fredriksson, Marcus Larsson, and Tomas Strömberg. Optical microcirculatory skin model: assessed by monte carlo simulations paired with in vivo laser doppler flowmetry. *Journal of biomedical optics*, 13(1):014015, 2008.